CHINESE OPTICS LETTERS

Vol. 22, No. 2 | February 2024

Photonic integrated optical phased arrays and their applications [Invited]

Zhipeng Ma (马志鹏)[1,2], Yuanjian Wan (万远剑)[1,2], Hang Liang (梁 航)[1,2], Yao Fu (付 瑶)[1,2], Guobiao Tang (唐国彪)[1,2], Xiaoyang Zhao (赵晓阳)[1,2], Shiao Zhao (赵世傲)[1,2], Haibo Kuang (匡海波)[1,2], Yu Zhang (张 宇)[1,2*], and Jian Wang (王 健)[1,2**]

[1] Wuhan National Laboratory for Optoelectronics, Huazhong University of Science and Technology, Wuhan 430074, China

[2] Optics Valley Laboratory, Wuhan 430074, China

*Corresponding author: yuzhang87@hust.edu.cn

**Corresponding author: jwang@hust.edu.cn

Received November 2, 2023 | Accepted January 22, 2024 | Posted Online March 1, 2024

In recent years, optical phased arrays (OPAs) have attracted great interest for their potential applications in light detection and ranging (LiDAR), free-space optical communications (FSOs), holography, and so on. Photonic integrated circuits (PICs) provide solutions for further reducing the size, weight, power, and cost of OPAs. In this paper, we review the recent development of photonic integrated OPAs. We summarize the typical architecture of the integrated OPAs and their performance. We analyze the key components of OPAs and evaluate the figure of merit for OPAs. Various applications in LiDAR, FSO, imaging, biomedical sensing, and specialized beam generation are introduced.

Keywords: optical phased arrays; LiDAR; silicon photonics; beam steering; photonic integration.

DOI: 10.3788/COL202422.020041

1. Introduction

The optical phased array (OPA) is a radiating array with an individually adjustable phase. By controlling the phase of each element, it is possible to achieve dynamic beam steering, arbitrary far-field imaging, optical wireless links, and so on. With the development of automatic driving, navigation technology enabled by sensors, including light detection and ranging (LiDAR), plays an important role, and OPAs also follow this trend. OPAs fabricated on integrated photonic platforms could lead to the next generation of solid-state LiDAR with reduced size, weight, power, and cost.

There are some early reports about liquid crystal OPAs[1,2]. Liquid crystal OPAs enable beam steering by loading the voltage on the liquid crystal molecules, but the device footprint is large, and the switching speed is relatively low. Photonic integrated OPAs, offer the advantages of small size, flexibility, and power conservation. Driven by the needs of low cost solid-state LiDAR, photonic integrated OPAs have attracted much research interest.

In this paper, we review the current progress of photonic integrated OPAs. In Section 2, we will introduce the typical architecture, including 1D, 1.5D, and 2D OPAs, and their performance. We will analyze the key components of the OPA, such as phase modulators and waveguide grating antennas, in Section 3. Section 4 will evaluate the figure of merit for OPAs used for LiDAR applications, and other applications will be discussed in Section 5. Finally, Section 6 will summarize and conclude the paper.

2. Review of Photonic Integrated OPAs

In terms of the architecture for OPAs, there are typically 1D OPAs, 1.5D OPAs, and 2D OPAs. Each of these structures has its own advantage. 1D OPAs are typically formed by an end-firing waveguide array and thus could perform beam steering in the lateral dimension only. By introducing diffractive gratings to the 1D waveguide array, beam steering in the other direction could be achieved by wavelength tuning. We define this architecture as 1.5D OPAs. For 2D OPAs, periodic array emitting elements are arranged along two different directions and thus could perform 2D beam steering via phase tuning only.

2.1. 1D photonic integrated OPAs

1D OPAs essentially refer to end-fire (EF) OPAs with power radiated from the facets of the waveguide array. Typically, the EF OPAs only enable 1D beam steering with a long and narrow light spot. Kossey *et al.* demonstrated an OPA with the emitting elements at the space of 775 nm (half-wavelength)[3]. The proposed 16-channel OPA is integrated on a 220 nm-SOI platform that is capable of edge emission of light with a measured lateral field of view (FoV) of up to 64°, as shown in Fig. 1. This OPA has potential in 1D beam steering applications for LiDAR.

Silicon is a transparent material at the infrared band but would cause extra loss at the visible spectrum. Silicon nitride (SiN) is an ideal platform for conducting visible operations with a wider transparent window. Figure 2 shows a chip-scale 1D

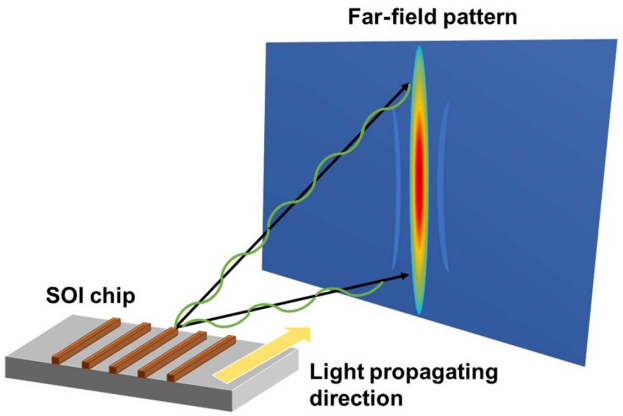

Fig. 1. Schematic of the 1D OPA and far-field pattern[3].

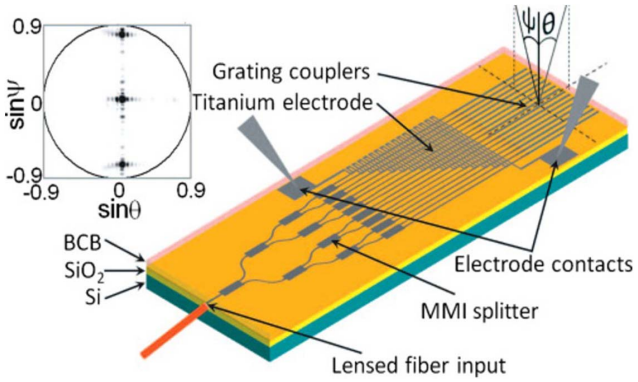

Fig. 3. 3D view of the 1.5D OPA[5]. The inset shows the far-field image.

OPA operating at a blue light wavelength (488 nm) using a SiN platform[4]. A 64-channel sparse aperiodic array OPA is used to adapt fabrication and achieve wide-angle beam steering over a 50° lateral FoV with a narrow beam divergence of 0.17°. The large-scale integration of a SiN platform paves the way for a fully reconfigurable chip-scale 1D LiDAR across the entire visible spectrum. However, SiN has a low thermo-optic coefficient and poor guide mode confinement. The 1D OPA has a narrow emitting aperture in the vertical direction, which causes a heavily divergent spot and a lower beam resolution. Thus, 1D OPAs cannot meet the growing demand of LiDAR, and the use of 2D beam steering is in response to the proper conditions and current trends.

2.2. 1.5D photonic integrated OPAs

We classify OPAs with lateral phase modulators and wavelength tuning by waveguide grating antennas (WGAs) as 1.5D OPAs, as 1D array structures achieve 2D beam steering. The phase modulator array manipulates the lateral wave front, while the WGAs couple light into free space and are scanned by wavelength tuning.

In 2009, the first integrated OPA on an SOI platform was reported by Acoleyen *et al.*[5], as shown in Fig. 3. They established the typical architecture of 1.5D OPAs. The proposed OPA chip consists of 16-channel WGAs with a 2 μm pitch. Steering in the lateral direction is done thermo-optically by titanium electrodes, while steering in the longitudinal direction is accomplished by wavelength tuning. They demonstrated lateral steering over an angle of 2.3°, and the wavelength tuning steering angle is 14.1° by WGAs.

Large-scale integration and full integration are promising trends for OPAs. The first fully integrated OPA chip using a hybrid silicon platform was reported by Hulme *et al.*[6]. It combined a large number of integrated components (164) on a silicon platform with integrated lasers and photodiodes. Hence, they achieved high-speed hybrid silicon distributed feedback (DFB) lasers, modulation, and detection in an OPA chip. The chip included two tunable lasers, 34 amplifiers, 32 photodiodes, 32 phase shifters, 31 MMI couplers, and a graded index (GRIN) lens on an SOI platform, as shown in Fig. 4. The GRIN lens images the remaining beam power into the far field measured by a photodiode array for on-chip feedback. The chip exhibited steering over 23° × 3.6° with a beam divergence of 1° × 0.6°.

Researchers at the Massachusetts Institute of Technology (MIT) have made great achievements in OPA LiDAR. Poulton *et al.* presented the first demonstration of a coherent solid-state LiDAR using OPAs in a silicon platform, which is able to measure distance and velocity while simultaneously using triangular frequency modulation, as shown in Fig. 5(c)[7]. Frequency-modulated continuous-wave (FMCW) LiDAR is utilized with a laser diode. They demonstrated the coherent LiDAR using a photonic integrated OPA chip and achieved distance and

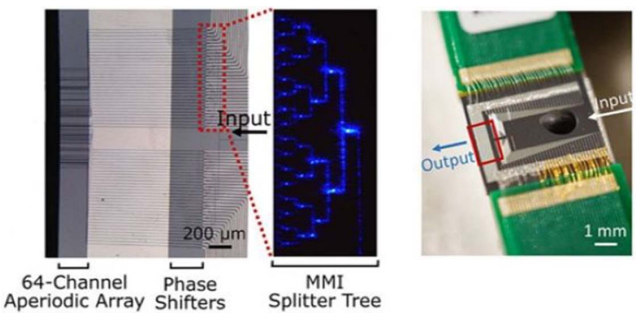

Fig. 2. Optical microscope image of 1D 64-channel OPA[4].

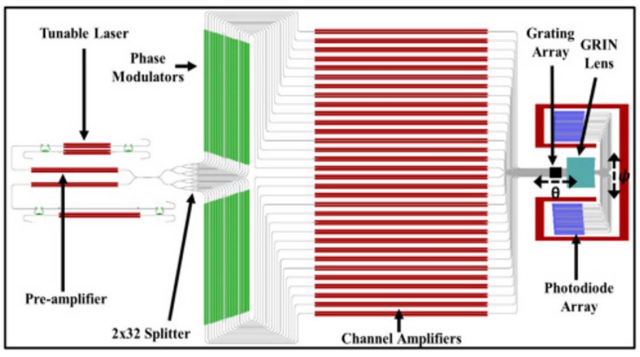

Fig. 4. Layout of the fully integrated OPA chip by UCSB[6].

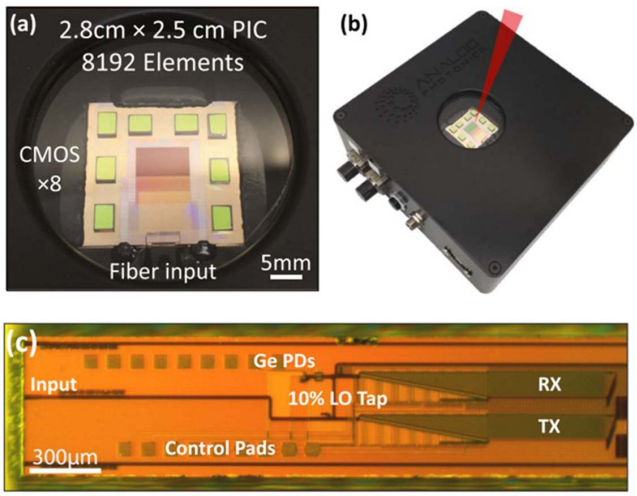

Fig. 5. (a) OPA PIC by MIT[8]. (b) Photograph of packaged OPA LiDAR[8]. (c) Optical micrograph of coherent solid-state LiDAR[7].

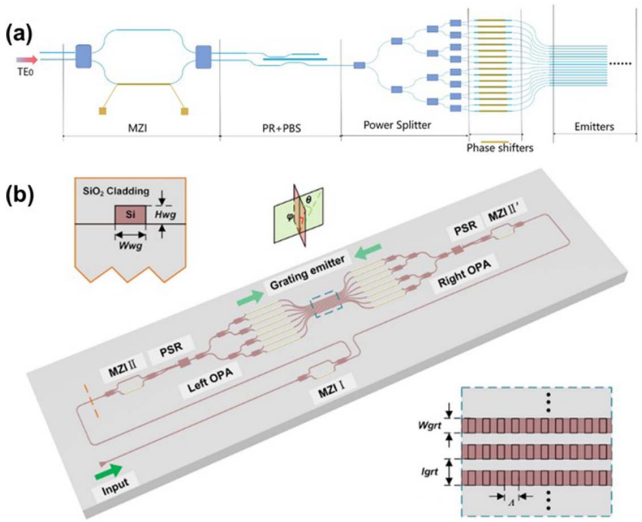

Fig. 6. (a) Schematic of the polarization multiplexed OPA[9]. (b) 3D view of the proposed bi-directional and dual polarization multiplexed OPA[11].

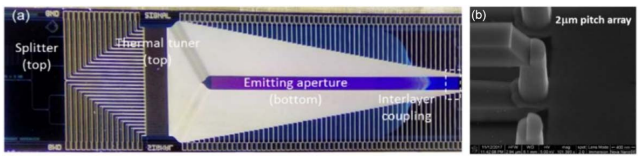

Fig. 7. (a) Layout of integrated silicon OPA chip[12]. (b) SEM image of the 3D interlayer coupler.

velocity measurements for the first time. Afterward, they reported an 8192-element OPA with individually addressed elements driven by custom CMOS electronics[8], as shown in Figs. 5(a) and 5(b). Eight CMOS DAC banks are flipped directly onto the PIC, which had a low power consumption of 2.5 W. A solid-state coherent LiDAR system is realized with transmitting/receiving OPAs coupled to an on-chip coherent receiver, driven by a low linewidth (50 kHz) laser. Phase shifters and vertical emitting antennas are narrowing to a 1 μm pitch, facilitating 2D beam steering with a 100° × 17° FoV. A narrow beam resolution of 0.01° × 0.039° is demonstrated with an 8 mm × 5 mm aperture. This high-performance demonstration brings a new era for OPA LiDAR technology. The proposed coherent 2D solid-state LiDAR can detect the range of nearly 200 m.

In addition, as the conventional wavelength tuning efficiency is near 0.14 deg/nm, thus the longitude steering angle is limited. Incidentally, the longitudinal steering angle can be expanded by multiplexing technology, such as polarization multiplexing[9] or direction-multiplexing[10]. Yan *et al.* proposed a double longitudinal steering angle OPA by polarization multiplexing. The TE_0 and TM_0 modes will diffract to the adjacent angle range, as shown in Fig. 6(a). The longitudinal steering range is doubled to 28.2° upon 100 nm wavelength tuning. Further, Zhao *et al.* designed a dual polarization multiplexed and bi-directional silicon OPA with a shared grating emitter array[11], as shown in Fig. 6(b). Two-stage MZI switches and polarization splitter-rotators are used to select the input directions and input polarizations. The simulation results show a 54.5° longitudinal scanning range upon 100 nm wavelength tuning. The longitudinal steering range is increased to nearly four times.

OPAs are moving toward large scale and multilayers. Zhang *et al.* proposed a large FoV (nearly 70°) and large-aperture active OPA[12], as shown in Fig. 7. The fabricated 24-element OPA has a 5-mm-long emitting aperture. The experiment shows 3.3° axial beam steering upon 20 nm wavelength tuning and >40° lateral beam steering with no sidelobe in a ±33° lateral FoV. They deposited 2 pairs of Si/SiO_2 distributed Bragg reflectors (DBRs) placed under the grating antenna array to reflect the undesirable downward power upward. Impressively, a 3D interlayer coupler is demonstrated for future 3D integrated OPAs.

SiN is an ideal auxiliary layer because of its lower transmission loss and there being no two-photon absorption (TPA) effect. Wang *et al.* at the Chinese Academy of Sciences (CAS) designed a SiN-Si dual-layer OPA chip fabricated on a SiN-on-SOI platform[13], which achieved a large two-dimensional scanning range of 96° × 14°, as shown in Fig. 8(b). The SiN input waveguide is able to handle large optical power and reduce transmission loss, hence providing a basis for long-range LiDAR. Phase modulators are still fabricated on silicon due to its high thermo-optical coefficient. Li *et al.* designed two kinds of 128-channel OPAs fabricated on a SiN-on-SOI platform[14]. They utilized two kinds of double-faced grating antennas to achieve high-emitting directivity. The fishbone antenna OPA achieves a 100° × 19.4° FoV with a beam divergence of 0.021° × 0.029°, and the chain antenna OPA realizes a 140° × 19.23° FoV with a beam divergence of 0.021° × 0.1°. They embedded the OPA chip into an FMCW system and detected the target at a distance of 100 m under 26 dBm input power, as shown in Fig. 8(a). Both of these two designs have taken advantage of the low transmission loss of SiN and the high modulation efficiency of silicon.

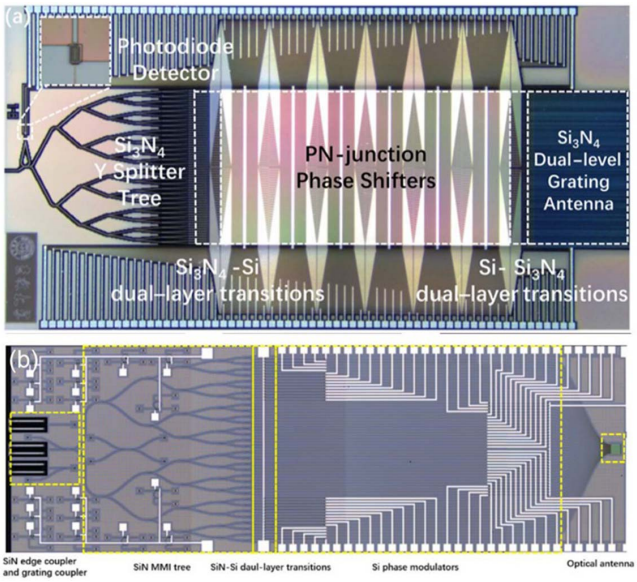

Fig. 8. (a) Optical micrograph of the wide steering angle SiN-Si dual-layer OPA by JLU[14]. (b) Optical microscope image of SiN-Si dual-layer OPA by CAS[13].

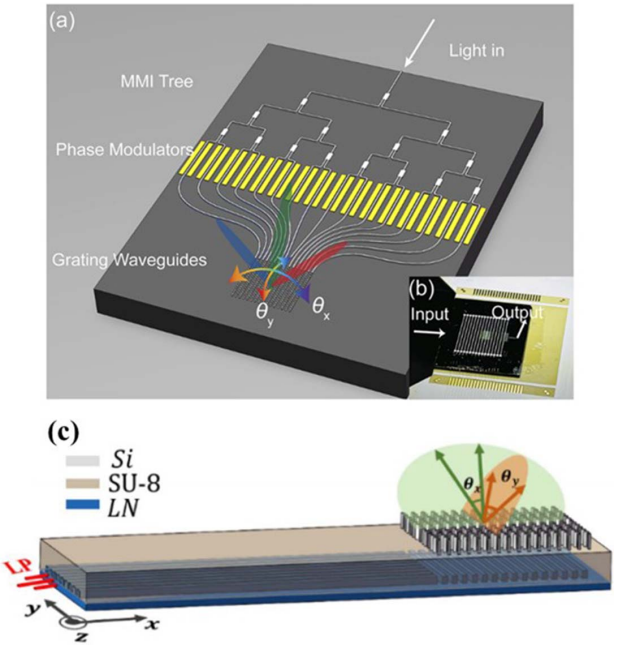

Fig. 9. (a) Schematic of the integrated LN OPA[15]. (b) Optical image of the LN OPA chip wire bonded to a PCB. (c) Scheme of the metasurface-integrated OPA[16].

Recently, thin-film lithium niobate (LN) is emerging as a material platform because it allows high-speed modulation, has low power consumption, and has low transmission loss. What is more, LN has various superior characteristics, such as an ultra-wide transparency window (400 nm–5 μm), a large electro-optic coefficient, a nonlinear-optic coefficient, an acousto-optic coefficient, and a pyroelectric coefficient. In 2023, Yue and Li reported an LN OPA[15], as shown in Fig. 9(a). They demonstrated a 16-channel 3-μm-pitch LNOI-OPA, appearing with a $24° \times 8°$ two-dimensional beam steering angle with a far-field beam divergence of $2° \times 0.6°$. Impressively, the power consumption of the phase shifter is as low as 13.5 pJ/π, which shows enormous potential in phase modulation. Incidentally, a metalens can also be integrated on OPAs as a steering range enlargement. Wang *et al.* designed an LN OPA with an integrated silicon metalens[16], as shown in Fig. 9(c). The silicon metalens above the OPA is designed according to the geometric Pancharatnam–Berry phase and enlarges the FoV. Experimental results demonstrate lateral beam scanning of ±21.27° and ±41.04° without and with a metalens. The metalens doublet design doubles the lateral scanning range.

2.3. 2D photonic integrated OPAs

We regard the 2D OPA with periodic elements as a real 2D structure, as it enables relatively symmetric beam steering by phase modulators in rows and columns. In a conventional 2D OPA structure, a great number of phase modulators are required to control every emitting element with a complex metal wire layout, thus affecting the element pitch. The research team at MIT implemented a large-scale (4096) 2D OPA and has proved the feasibility of the 2D OPA technology for advanced LiDAR applications[17]. In addition, the 64×64 antenna arrays of the OPA are integrated on a silicon chip, while the device size is only $576\ \mu m \times 576\ \mu m$. They also demonstrated a simplified 8×8 active OPA. The phase difference in the rows and columns is controlled by a thermal phase shifter array, as shown in Fig. 10. With dependent phase control and with the full CMOS circuitry to access all of the pixels, the far-field patterns can be adjusted dynamically.

Unfortunately, 2D OPA has the inherent defects of complexity and large power consumption, as every element pixel requires a phase modulator to form the phase difference in the rows and columns. To solve this deficiency, Ashtian *et al.* proposed a new 2D OPA framework. They reported an $N \times N$ OPA, where only $2N$ phase shifters are needed, which significantly reduced the total power consumption and eliminated electrical routing[18]. An 8×8 OPA that uses 16 phase shifters to perform 2D beam

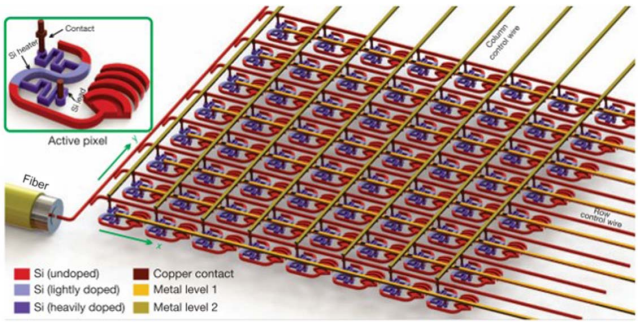

Fig. 10. (a) Schematic illustration of the 8×8 active OPA by MIT[17]. The phase of each pixel is continuously tuned by thermo-optic effect through an integrated doped heater.

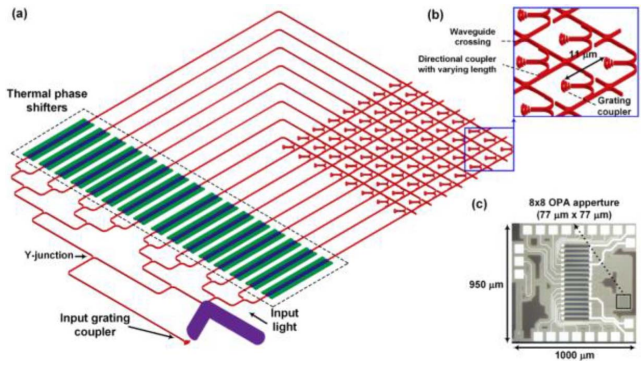

Fig. 11. (a) Structure of the implemented 8 × 8 OPA with 16 phase shifters[18]. (b) Structures of the grating couplers and directional couplers. (c) Microphotograph of the implemented 8 × 8 OPA chip.

steering without tuning the wavelength is implemented. Using the aperture size of 77 μm × 77 μm for the implemented OPA transmitter, far-field beam-steering over a range of about 7° is demonstrated, as shown in Fig. 11. A comparison for the OPAs is shown in Table 1. We mainly compare the 1.5D OPAs and the 2D OPAs. The 1.5D OPAs seem to be more in line with the LiDAR requirements. It is obviously because 2D-OPAs suffer from a large element pitch, and the FoV is limited.

2.4. 2D switch array LiDAR

In addition, there is another method for achieving 2D beam steering with a switch array. 2D beam steering, known as focal plane array LiDAR, is mainly achieved by using 2D switch arrays. The on/off states of the switch arrays are mainly adjusted by electric signal. Rogers *et al.* have demonstrated a scalable solid-state 3D imaging LiDAR that achieves a range of >70 m[19]. This system meets the needs of applications like solid-state 3D imaging and LiDAR. The advantages of long range and eye safety are meaningful in this system. This result paves the way for low-cost, compact, and high-performance 3D imaging cameras that could be used in robotics and autonomous navigation, as shown in Fig. 12.

What is more, Zhang *et al.* have presented a 16,384-pixel imaging LiDAR using a 128 × 128 silicon photonic focal plane switch array (FPSA), in which a 128 × 96 subarray is wire bonded and tested in experiments[20], as shown in Fig. 13. The grating antenna in each pixel is digitally controlled by an integrated MEMS optical switch. Random-access beam steering with an FoV of 70° × 70°, an addressing resolution of 0.6° in both directions, a beam divergence of 0.05°, and a sub-MHz operation speed is achieved with a 5-mm-focal-length imaging lens. 3D imaging with a 1.7 cm range resolution has also been demonstrated. The angular resolution of the current system can be further increased by optimizing the optical design and fabrication technology.

3. Key Components of Photonic Integrated OPAs

Devices in large-scale OPAs include but are not limited to optical couplers, optical switches, beam splitters, phase modulators, optical amplifiers, and emitter gratings. We aim at LiDAR applications with a high frame rate, a high output power, and an

Table 1. The Performance Comparison of Some OPAs.

References	Year	Array Size	Platform	Dimension	Steering Angle (°)	Beam Resolution (°)	Pitch (μm)
[5]	2009	1 × 16	SOI	1.5D	2.3 × 14.1	2.5 × 2.7	2
[21]	2011	1 × 16	SOI	1.5D	23 × 6.7	1.27 × 2.8	5
[6]	2015	1 × 32	III-V/Si	1.5D	23 × 3.6	1 × 0.6	4
[7]	2017	1 × 32	SOI	1.5D	46 × 36	0.8 × 0.16	2
[22]	2019	1 × 512	SOI	1.5D	56 × 15	0.04	1.65
[12]	2019	1 × 120	SOI	1.5D	40 × 3.3	N/A	1.3
[23]	2020	1 × 512	SOI	1.5D	70 × 6	0.15 × 0.08	1.3
[13]	2020	1 × 1024	SiN-on-SOI	1.5D	96 × 14	2.3 × 2.8	1.65
[15]	2023	1 × 16	LNOI	1.5D	24 × 8	2 × 0.6	3
[24]	2010	4 × 4	SOI	2D	1.5	9.6 × 4.8	87.2 × 72.2
[17]	2013	64 × 64	SOI	2D	6 × 6	N/A	9 × 9
[25]	2015	8 × 8	SOI	2D	1.6 × 1.6	N/A	33 × 33
[18]	2019	8 × 8	SOI	2D	7 × 7	N/A	11 × 11

Table 2. The Contrast of Phase Modulators for OPAs.

References	Year	L (μm)	P (mW)	Type	Bandwidth (Hz)
[4]	2020	300	30	TO	~5000
[5]	2009	/	8.2	TO	/
[6]	2015	/	160	EO	5×10^7
[14]	2021	7000	0.0018	EO	/
[17]	2013	/	8.5	TO	/
[15]	2023	10,000	/	EO	4.2×10^9

ultra-sharp instantaneous field of view (IFoV). Hence, our focus is mainly on the last three devices.

3.1. Phase modulator

Phase modulators are operated to provide local heating [Fig. 14(a)] or to apply a voltage to the waveguide [Figs. 14(b)–14(d)], thus thermo-optically or electro-optically adjusting the effective index of the guide mode. In this way, lateral beam steering is achieved. Phase modulators on silicon photonic chips are mainly adopted using two different theories: the thermo-optic (TO) effect and the electro-optic (EO) effect.

Silicon has a relatively high TO coefficient nearing a 1.55 μm wavelength, as a value of $1.86 \times 10^{-4}\ \mathrm{K}^{-1}$. Silicon TO phase modulators are widely implemented to manipulate the phase in OPAs due to the low loss. While the TO coefficient of SiN is only $1.7 \times 10^{-5}\ \mathrm{K}^{-1}$, the SiN TO phase modulation will thus lead to high power consumption and low modulation efficiency[4]. What is worse, due to the TO response for warming and cooling, the bandwidth of the TO modulation is limited to about 100 kHz.

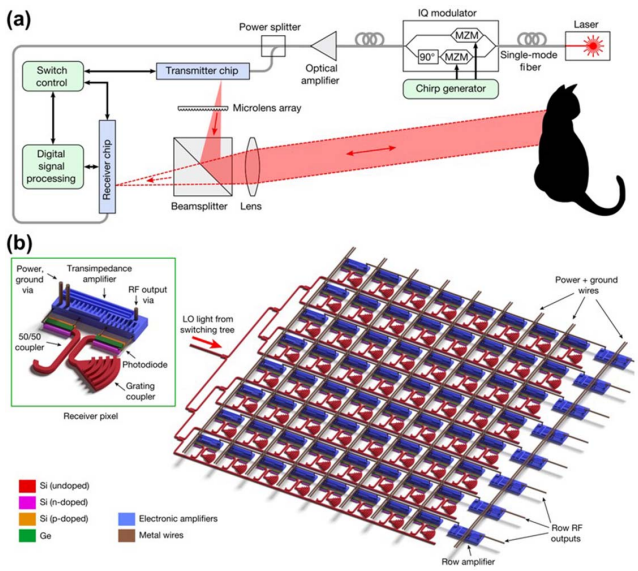

Fig. 12. (a) Schematic of the solid-state 3D imaging LiDAR[19]. (b) Schematic of a receiver block in receiver focal plane array (FPA).

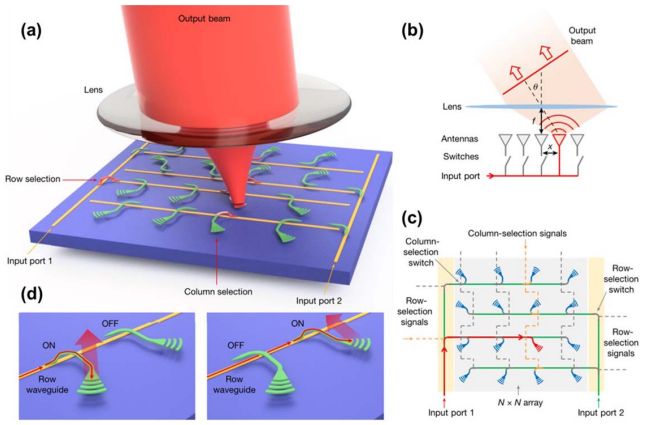

Fig. 13. (a) Perspective view schematic of the focal plane switch array (FPSA)[20]. (b) Schematic of a 1D beam scanner. (c) Top-view schematic of the focal plane switch array design. (d) Schematics of the MEMS optical switches and grating antennas in the on/off states.

EO phase modulation has faster modulation speeds, which is a more efficient method for phase modulation[26]. EO phase modulators utilize the plasma dispersion effect, carrier injection or carrier depletion in the silicon waveguide. In carrier injection (p-i-n) EO phase modulator, when a forward voltage is applied across the device, free electrons and holes will be injected into the intrinsic region and change the effective refractive index. Carrier depletion is another scheme used to control the carrier density, which is of a mainly p-n diode structure. The effective index is changed with the depletion width varying due to the reverse voltage. Although a p-n diode structure has a larger bandwidth, the p-i-n diode structure is more suitable for OPA chips for the lower optical loss.

Heterogeneous III–V/Si phase modulators can overcome above performance trade-offs in phase modulators[27], which can comprehensively improve OPA performance. Since III–V material has an additional modulation effect to increase the total

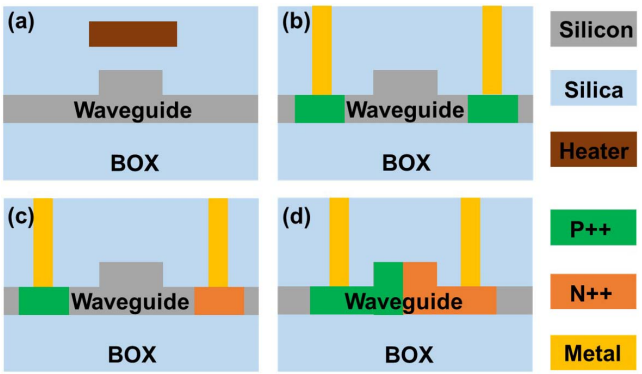

Fig. 14. Schematics of different phase modulators. (a) Directly resistor heated TO phase modulator. (b) Resistor heated TO phase modulator. (c) Carrier injection (p-i-n) EO phase modulator. (d) Carrier depletion (p-n) EO phase modulator.

effect, the higher electron mobility in III–V material promotes wider bandwidth and lower carrier absorption[28]. Table 2 summarizes some key performance merits for phase modulators used in OPAs.

3.2. Emitter grating

The transmitter and receiver apertures consist of a grating antenna array. Therefore, a high-performance emitter grating can help the OPA to realize a high spot resolution. There are some design methods of grating antennas, like uniform emission, multilayer unidirectional emission, and slow-light grating.

The uniform emission can be achieved by the apodized grating, which is size-variable along the transmission direction to fit the uniform near-field intensity distribution. Shang *et al.* reported uniform propagation constant silicon gratings for beam steering applications with ultra-sharp IFoV[29]. To achieve uniform emission intensity with a relatively long emission length, they designed a custom grating with varying SiN widths and duty cycles, thus maintaining a uniform propagation constant, as shown in Figs. 15(a) and 15(b). They fabricated the custom grating with the varying SiN width/duty cycle. The proposed grating demonstrated a beam steering angle of 6.6° by wavelength tuning from 1530 to 1575 nm with the emission length over 1 mm. The measured far-field 3 dB beam divergences for TE_0 mode are 0.10° and 0.75° for the custom grating and reference grating, respectively. Yu *et al.* also demonstrated a large effective emitting length SiN apodized grating antenna with a fishbone shape[30]. They utilized an OPA chip with apodized grating to achieve 100 m distance in the ranging experiment with a small divergence of 0.05° × 0.04°. They found that the effective aperture of the apodized grating antenna is about twice that of the uniform grating antenna. Therefore, the main benefit of uniform emission grating antennas is a lower beam divergence with the same aperture. In other words, the effective aperture of the apodized grating is larger than that of the uniform grating, thus increasing beam resolution.

Another design method is the multilayer unidirectional emission grating. A multilayer structure enables vertical interference or semiconductor reflector. In this way, high directivity emission can be achieved. Raval *et al.* demonstrated millimeter-long waveguide grating antennas with unidirectional emission for integrated OPAs[31]. Unidirectional emission eliminates the blind spots caused by reflections within the substrate. Over 90% directionality is demonstrated by double-deck SiN layers, which allow for a high effective aperture and emission efficiency. These antennas are useful for integrated OPAs with high transmission output power and high receiving efficiency for LiDAR and FSO systems. The structure is shown in the Fig. 16(d).

To achieve a 5-mm-length and high efficiency grating antenna, a low-contrast SiN-assisted grating design was reported in Ref. [12], as shown in Figs. 16(a)–16(c). They designed and deposited two Si/SiO_2 distributed Bragg reflector (DBR) layers placed under the grating antenna layer to reflect the undesirable downward emission upward. Thus, downward emission is suppressed, and a unidirectional emission characteristic can be achieved with more than 90% efficiency. As the designed DBR has a broad reflection band and is less sensitive to the layer thickness variation, the result shows > 94% reflectance for two DBR layers, while only 46% can be achieved without the DBR. To achieve a large emitting aperture over a 5 mm length, a weak emitting structure using SiN-assisted waveguide gratings was used. The measurement shows an emission rate of 23 dB/cm (~95% power emitted over the 5 mm length).

Slow light can be achieved in a 1D and 2D photonic crystal structure. The large group index of slow light improves the steering sensitivity. Suyama *et al.* proposed a high-efficiency, slow-light grating antenna enabled by a photonic crystal consisting of through-hole grating and surface grating, which selectively radiate upward[32], as shown in Fig. 17. Via the optimization using the covariance matrix adaptation evolution strategy, they achieved a slow-light grating structure showing a maximum upward emissivity of 95% as well as moderate radiation rates and beam divergence. Experimentally, the emissivity was enhanced

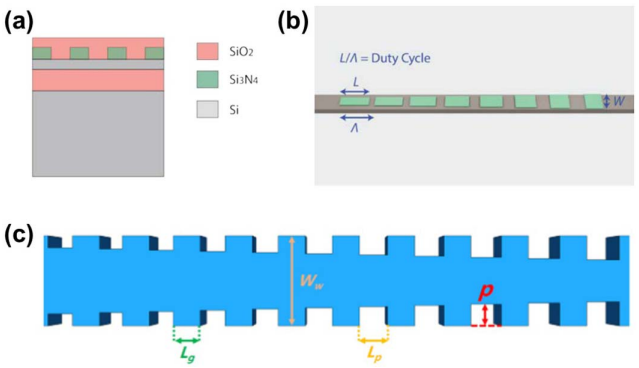

Fig. 15. (a) The cross section and (b) schematic of the proposed uniform propagation constant SiN/Si grating[29]. (c) Schematic of the SiN apodized grating antennas[30].

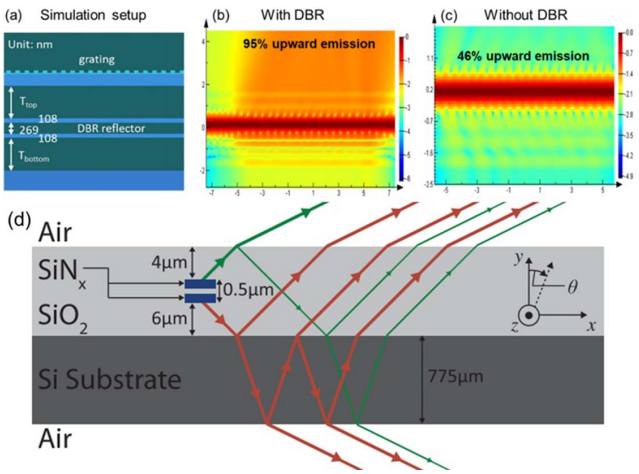

Fig. 16. (a) Schematic of the grating antenna with DBR[12]. Simulated grating emission profile (b) with and (c) without bottom DBRs. (d) Schematic of unidirectional WGA by MIT. The figure shows multiple reflections in the silicon substrate and overlying photonic layer stack[31].

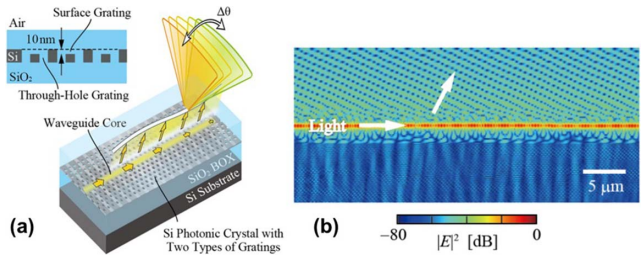

Fig. 17. Schematic of the single slow-light grating antenna[32].

by 2–4 dB, which is significant in applications to LiDAR applications.

3.3. Optical amplifier

Because of the high loss of OPAs and the low input power limited by the two-photon absorption (TPA) of silicon, it is necessary to compensate for the channel power by using a semiconductor optical amplifier (SOA). The integrated SOA depends strongly on low-loss and low-reflection mode converters. In Ref. [33], a high-gain SOA is proposed and is used as a pre-amplifier. The transition between the passive silicon waveguide and the hybrid waveguide of the amplifier is formed by adiabatic tapers. For a 1.2-mm-long structure, the maximum gain is 9.5 dB at 300 mA.

The pre-amplifiers in Ref. [6] are made with 1.5-mm-long structures for amplification of the signal prior to entering the splitter, and the channel amplifiers were made to be 3 mm long to maximize the output power. It was expected that increasing the length of the pre-amplifier beyond 1.5 mm would not significantly increase the gain due to the saturation of the SOA. The decreased signal following the splitter is expected to see a linear gain in the 3 mm amplifiers.

4. Evaluation of Integrated OPAs

The parameters of the OPAs will directly affect the LiDAR performance. In this section, evaluation criteria of the OPAs are discussed, which are FoV, link loss, detection range, beam divergence, and side lobe suppression ratio (SLSR). Lateral FoV is supposed to be at least 120° when LiDAR is attached to the front and rear headlamps, whereas the vertical FoV is typically 30°–40°. The total losses of the OPAs need to be further reduced to meet the long-range measurement. To reach the Level 4 requirements of autonomous driving technology, the forward measurement range should be over 250 m, with the ranges of ~100 m and ~40 m for the rear and side scanning, respectively[34]. A narrow beam divergence is positively related to the effective aperture and determines the LiDAR system resolution. A high SLSR is beneficial to a large FoV measurement.

4.1. Beam steering angle

Longitudinal steering angle θ is changed by incident light wavelength tuning. The emitting beam angle θ is expressed by

$$\sin\theta = \frac{\Lambda n_{\text{eff}} - \lambda_0}{\Lambda n_{\text{back}}}, \tag{1}$$

where θ is the longitudinal steering angle, Λ is the period of the diffraction grating antennas, λ_0 is the incident wavelength, n_{eff} is the effective index of the mode in the gratings, and n_{back} is the background refractive index.

Phase modulators manipulate the wavefront and achieve lateral beam steering. Lateral steering angle Ψ is similar to the microwave phased array principle. The lateral outcoupling angle Ψ of the OPA with spacing d is given by

$$\sin\Psi = \frac{\lambda_0 \Phi}{2\pi d}, \tag{2}$$

where Ψ is the lateral steering angle, λ_0 is the incident wavelength, and Φ is the uniform phase difference between the emitter arrays. Narrowing the pitch of emitter array can enlarge the FoV but lead to higher crosstalk as well. The maximum scanning angle range of the OPAs is related to the pitch of the emitter array. In order to avoid crosstalk between the waveguide array, the antenna pitch can be set to more than a wavelength. However, a large array pitch will severely limit the scanning range of the OPAs. As a consequence, we should make a trade-off between the FoV and crosstalk. For high-density OPAs, Song *et al.* proposed the waveguide superlattices interlacing-recombination method, a supercell comprising a sub-array of waveguides. Due to the severe phase mismatch between the adjacent waveguides, the crosstalk of the intra-supercell and the inter-supercell is suppressed[35]. That paves a way for half-wavelength pitch OPAs[36]. However, the difference in the effective index causes extra phase calibration in the experiment. In addition, an alternative solution is a nonuniform sparse array[14], which is a promising approach for achieving wide steering range, low array crosstalk, and large aperture simultaneously. The nonuniform-pitch OPAs are aliasing-free in the entire FoV and thus realize a wide steering range. However, the far-field main lobe power becomes lower, thus leading to extra loss in the far-field spot.

As mentioned in Section 2.2, polarization multiplexing and direction multiplexing are solutions that improve the vertical steering angle. Researchers at Zhejiang University reported on these two methods. The OPA with polarization multiplexing[9] has twice the longitudinal scanning angle contrast with one polarization mode. The simulation result shows 28.2° longitudinal beam steering via wavelength tuning, as shown in Fig. 6(a), while the polarization multiplexed and bi-directional OPA shows a 54.5° longitudinal scanning range upon 100 nm wavelength tuning. A slow-light grating antenna is also an alternative method, as discussed in Section 3.2.

4.2. Link budget

In order to calculate the efficiency and total loss of the OPA, we adopt a 1×16 OPA structure. Assume that the input power from the laser and the SOA is 100 mW. Table 3 shows the loss

Table 3. Link Budget.

Element	Loss Type	Typical Value (dB)	Efficiency	Power (mW)
Edge coupler	Coupling loss	2	63%	63
Waveguide	Transmission loss	2	63%	40
1 × 16 splitter	Excess loss	1	80%	32
EO p-i-n modulator	Insertion loss	3	50%	16
Grating array	Excess loss	1	80%	12.8
Grating array	Downward emission loss	3	50%	6.4
Total	Link loss	12	6.4%	6.4

of every component. In this way, the final efficiency of 6.4% is obtained.

There are some methods that reduce transmission loss and improve efficiency. For example, we can use an on-chip light source to avoid fiber-to-chip loss. The SOA is able to compensate for the channel power. In addition, the DBR is supposed to reflect the undesirable downward emission upward. SiN is also a superior material that supports high optical power, thus enabling long-range measurement.

4.3. Detection range

Conventionally, the distance measurement principle of LiDAR is the time-of-flight (ToF) method, which can be defined as

$$R = \frac{ct_p}{2}, \tag{3}$$

where R is the distance between the target and the transmitting aperture, c is the speed of light in vacuum, and t_p is the time interval. In order to improve the detection range, it is necessary to increase the transmission power into the chip. The power threshold is about 16–19 dBm, which restricts the energy input of the laser into the chip. The LiDAR equation is given by[7]

$$P_R = P_T \eta_{\mathrm{TX}} \frac{\rho A_{\mathrm{RX}}}{4\pi L^2} \eta_{\mathrm{RX}}, \tag{4}$$

where P_R is the received power, P_T is the transmitting power, ρ is the reflectivity of the target, A_{RX} is the receiver area, L is the distance to the target, and η_{TX} and η_{RX} are the efficiency of the TX and RX. Equation (4) shows that, to receive more optical power, a large RX aperture is needed. Assuming that $\rho = 100\%$, $L = 200\,\mathrm{m}$, $P_T = 100\,\mathrm{mW}$, $A_{\mathrm{RX}} = 1\,\mathrm{cm}^2$, and $\eta_{\mathrm{TX}} = \eta_{\mathrm{RX}} = 6.4\%$, we can calculate that the received power is 0.819 fW. As a result, we find it too weak to meet the requirements of automatic driving. SOAs are supposed to compensate for the optical power of the channel array.

In fact, it is hard to detect tiny optical powers. In Ref. [7], coherent detection utilizes an on-chip LO for amplification, which allows for the use of standard germanium photodetectors. The initial system shown employed FMCW LiDAR with triangular frequency modulation and achieved simultaneous distance and velocity measurements with a 2-m range and a resolution of 20 mm. Frequency modulation was realized by manipulating the injection current of an off-chip compact laser diode. After the demonstration of this system, OPAs were added as a TX and RX in the FMCW LiDAR. The OPAs utilized a grouped cascaded phase modulators architecture for simple control. The beam was steered to three targets, and their distances were measured up to 0.5 m.

Autonomous driving technology is broken down into 5 levels[34], depending on the degree of human intervention. To meet the Level 3 or higher requirement, the measurement range should be 100–200 m. The distinguishing ability is supposed to reach 10 cm in size. The FoV of the LiDAR should be at least 120° × 30°. According to the ToF ranging principle, if we need a ranging length of 250 m, then the decision time of the LiDAR needs to be shorter than 0.83 μs to avoid dangers. In FMCW LiDAR, according to the relationship between coherent length l and laser linewidth $\Delta\lambda$ in Eq. (5), if the detection length is 40 m, 100 m, 200 m, and 250 m, then the laser linewidth should be at least 1193 kHz, 477 kHz, 238 kHz, and 191 kHz. In addition, coherent detection has an advantage of achieving local optical amplification so that it provides coherent gain, as calculated in Eq. (6), where P_s is the received optical power, P_{lo} is the local optical power, and φ_0 is the initial phase difference of the received optical signal and the local optical signal,

$$l = c \times \Delta t = \frac{\lambda^2}{\Delta\lambda}, \tag{5}$$

$$I(t) = 2R\sqrt{P_s P_{\mathrm{lo}}}\sin(\Delta\omega t + \varphi_0). \tag{6}$$

4.4. Beam divergence

The beam divergence is inversely proportional to the total aperture size of the array and the cosine of the steering angle Ψ[5],

$$\Delta\theta = \frac{0.886\lambda_0}{Nd\cos\Psi}, \tag{7}$$

where $\Delta\theta$ represents the full-width at half-maximum (FWHM) of the main lobe, and N is the number of the antennas. Equation (7) shows that the beam width is determined by the aperture of the optical aperture. A narrow beam spot can be realized by increasing the number of array channels in the OPAs. It is noted that a large beam steering range requires a narrow optical antenna pitch, while a narrow beam spot can be reached with a large optical antenna pitch. Therefore, it is essential to keep the antenna spacing in an optimal value[37]. The beam steering angle can be increased by reducing the period of the waveguide arrays. A compromise is supposed to be made between the FoV and the beam divergence because the number

of addressable spots depends on the number of radiating elements of the OPAs.

In Ref. [21], the sidelobe level is reduced by 13 dB. The FoV was 23° using a 4-μm-wide antenna array spaced at 5 μm. The different output orders of the array were spaced at 18°. This FoV and output order spacing could easily be increased by decreasing the waveguide width and pitch, respectively, but will result in a broader beam as the number of elements stays constant. The beam divergence was 1.27°. Using TO phase modulators, the beam was steered over its complete FoV. In Ref. [38], the control signals for the optical variable phase shifters and attenuators are provided by 136 DACs with a 14-bit nonuniform resolution using 2.5 V input–output transistors. The implemented OPA can create 0.03° narrow optical beams that can be steered unambiguously within ±22.5°.

4.5. Side lobe suppression ratio (SLSR)

When the waveguide width is constant, the period of the waveguide array mainly affects the position of the far-field side lobes. The larger the period of the array element, the closer the side lobe is to the main lobe, and it has a limited scanning angle of OPAs. However, if the array element period is too small, crosstalk will significantly increase between the adjacent waveguides, which affects the transmission characteristics of the beam spot in the OPAs, thus affecting the imaging quality of the far-field.

OPAs can be regarded as diffraction grating arrays and are essentially multi-beam diffraction systems. The basic theory of OPA technology is similar to Fraunhofer multi-slit diffraction. By controlling the phase difference of the beam in the adjacent waveguides, they have the same phase in a fixed direction. In this direction, the far-field intensity is the highest, and the destructive interference will occur in other directions.

Qiu *et al.* reported a high SLSR OPA in both two orthogonal directions[39]. They proposed a Y-splitter-assisted cascaded coupling array to realize the Gaussian power distribution of the array channel in the azimuthal direction, which significantly increases the SLSR from 20 to 66 dB in theory. In the polar direction, they designed an apodized grating antenna to realize the Gaussian power distribution. Based on both designs, they experimentally demonstrated a 120-channel OPA with dual-Gaussian power distribution in both two orthogonal directions, as shown in Fig. 18. The SLSRs in the φ and θ directions are measured to be 15.1 dB and 25 dB, respectively.

Assume that a one-dimensional uniform OPA is composed of N arrays and the array spacing is d. On the basis of the optical far-field diffraction theory, the field strength formula at point p can be obtained,

$$E(p) = \sum_{n=0}^{N-1} E_n(p) = \sum_{n=0}^{N-1} A_n e^{-jn\Delta\varphi} \frac{e^{-j\frac{2\pi}{\lambda}r_n}}{r_n}, \tag{8}$$

where λ is wavelength of incident light, r_n is the distance from the array to the observation point p, A_n is the amplitude of the

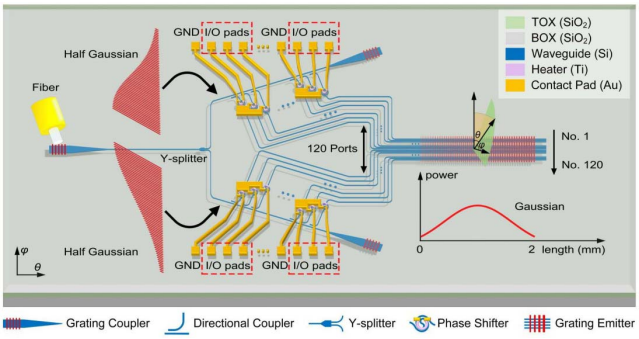

Fig. 18. Schematic of high-SLSR Gaussian power distribution OPA[39].

nth array, and $\Delta\varphi$ is the phase difference between the adjacent arrays.

In Eq. (9), since $|\sin\theta| \le 1$, when $d \ge \lambda$, no side lobes will be generated, i.e., when the beam is not deflected, no side lobes will be generated,

$$d \le \frac{\lambda}{1 + |\sin\theta_s|} \le \frac{\lambda}{2}, \tag{9}$$

where θ_s is the OPA beam pointing angle. Therefore, the array spacing can be shortened to half a wavelength to avoid side lobes, but too close a distance between the arrays will cause large crosstalk, and the array structure needs to be optimized[3,40].

The unequally-spaced array element distribution is a commonly used method to eliminate side lobes in the OPA[41,42]. Its essence is to change the phase difference between the adjacent elements. It is also possible to add a non-periodic phase to the original periodic phase to achieve the purpose of changing the phase[43]. Phase control signals are added to each array element to change the phase of the emitting beam so that the original periodic phase difference is changed, and the periodic phase is changed to a non-periodic phase through the control signal. In this way, the original side lobe cannot meet the condition of constructive interference due to the modulation of the non-periodic phase, thus achieving the purpose of suppressing the grating lobe.

In a word, optimizing SLSR is extremely important. Side lobes radiate power in unwanted directions, causing increased crosstalk between waveguides. Enlarging the angle between two consecutive lobes requires narrowing the antenna spacing. Another approach to increase SLSR is to vary the emitter spacing. In Ref. [6], they used a Gaussian distribution for waveguide pitch, which resulted in a different side mode profile, with the first major side lobe reduced to the level of the other side lobes. The Gaussian array is more uniform across the tuning space with a much better SLSR, and the main lobe contains 48% at 0° with an SLSR of 13.9 dB. In Ref. [21], by making use of a star coupler, they achieved a natural apodization of the field over the OPA, and the simulation showed a sidelobe level decrease.

5. Applications

Drawing upon the array of enhancement strategies mentioned earlier, significant strides have been made in augmenting the performance of large-scale OPA systems, rendering them markedly superior and more pragmatic. These large-scale OPAs, characterized by their adeptness in swift manipulation and dynamic beam steering, transcend their role in facilitating the miniaturization of laser radar systems. They also provide chip-level solutions applicable to diverse scenarios, including LiDAR, FSO, imaging, biological sensing, and specialized beam generation.

5.1. LiDAR

The LiDAR application is an ideal stage for OPAs. Today, with the development of automatic driving, navigation technology plays an important role nowadays. LiDAR can help achieve it. Early LiDAR systems were large mechanical equipment, consisting of a variety of components. Mechanical LiDAR has inherent disadvantages, such as slow scanning speed, large volume, and poor stability, which cannot meet the LiDAR requirements of reliability and long life. Compared with the traditional mechanical scanning devices, OPAs have the advantages of fast scanning rate, low power consumption, compact size, and high resolution.

Zhang *et al.* fully packaged their OPA device[12] into a computer controlled 2D beam steering system. Figure 19(a) shows a zoom-in of the packaged 120-channel OPA chip on a PCB. Following beam calibration, they demonstrated 2D optical beam steering through tuning the OPA phase for lateral beam steering and tuning wavelength for longitudinal beam steering. Figure 19(b) shows a composite photo of over 100 far-field beam patterns trained in forming the Lockheed Martin logo.

Zhou *et al.* reported a fully integrated LiDAR transmitter based on the multi-layer platform[44], as shown in Fig. 19(c). Due to the high-power handling of the SiN external cavity, an on-chip lasing output of 18 mW is achieved. The device exhibits an on-chip insertion loss below 3 dB together with a platform-record beam divergence of $0.051° \times 0.016°$. Two-dimensional patterns such as the 'SJTU' logo are demonstrated, as shown in Fig. 19(d).

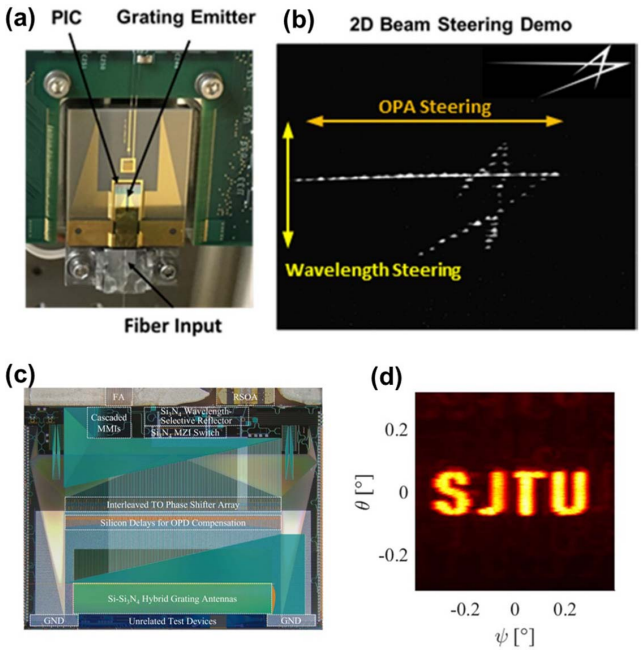

Fig. 19. (a) Fully packaged coherent OPA chip on the PCB[12]. (b) Composite IR image for the scanning spots. (c) Photo of the solid-state OPA[44]. (d) 2-D beam steering displaying the 'SJTU' logo.

5.2. Free-space optical communication

In the development of FSO systems, beam control has always been considered a crucial component. Large-scale OPA technology offers an efficient means for achieving non-mechanical beam control, contributing to the reduction of system size and power consumption.

Chow *et al.* have proposed and demonstrated an integrated active control OPA in optical wireless communication (OWC) systems[45], as shown in Fig. 20(a). They employed a genetic algorithm (GA) to optimize the voltages of 30 phase shifters to generate low-divergence beams in different directions. This was validated by transmitting a 10 Gb/s OOK signal, successfully achieving signal transmission. Furthermore, Li *et al.* utilized an integrated silicon-nitride OPA chip, displaying a high-data-rate and long-distance optical wireless communication system[46], as depicted in Fig. 20(b). They achieved reduced beam divergence using a 128 nonuniform-space waveguide grating antennas array, enabling 32 Gb/s NRZ signal transmission over a 54-m free-space distance and over 50 Gb/s PAM4 signal transmission within a 10-m range. Additionally, they also demonstrated the flexibility of multi-target communication in an OWC system based on OPA.

These research achievements highlight the promising applications of large-scale OPA technology in the field of optical

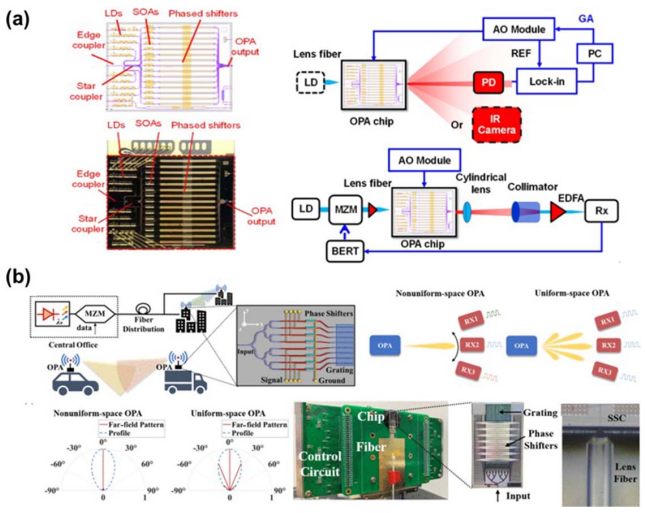

Fig. 20. (a) Integrated actively steerable OPA chip for optical wireless communication[45]. (b) Nonuniform-space OPA for optical wireless communication[46].

wireless communication, offering innovative solutions for improving communication performance and flexibility.

5.3. Imaging

Large-scale OPA technology possesses outstanding control capabilities, enabling precise phase, intensity, and direction control at the individual pixel level. This technology provides an efficient avenue for downsizing optical imaging systems.

In the field of projection systems, Aflatouni *et al.* proposed an integrated projection system based on a two-dimensional OPA[47], as depicted in Fig. 21(a). This system boasts rapid beam control capabilities. In this setup, the phased array units employ forward-biased p-i-n phase modulators, enabling swift phase control. By combining optimization algorithms, comprehensive phase compensation control is achieved. Images were generated and recorded in an infrared camera by using the rapid vector scanning technique. In the context of ghost imaging (GI) applications, Kohno *et al.* utilized integrated OPAs to successfully retrieve a slit pattern with over 90 resolvable points in one dimension[48]. Additionally, they harnessed wavelength control to achieve 2D imaging capabilities, as illustrated in Fig. 21(b). Yoon *et al.* demonstrated a high-accuracy 3D imaging system using a silicon OPA with thermo-optic tunable antennas[49]. The proposed OPA achieves a 45° × 10° FoV with a beam divergence of 0.7° × 0.6°. In addition, they used a ToF approach for distance measurement and showed a 2 cm ranging accuracy.

They provide robust support for innovation and miniaturization in optical imaging systems, opening up new prospects for the future development of optical imaging and projection technologies.

5.4. Biological sensing

The capabilities of on-chip OPA chip-level optical systems, especially within the visible spectrum, for biological applications, particularly in the field of neuroscience, to achieve deep

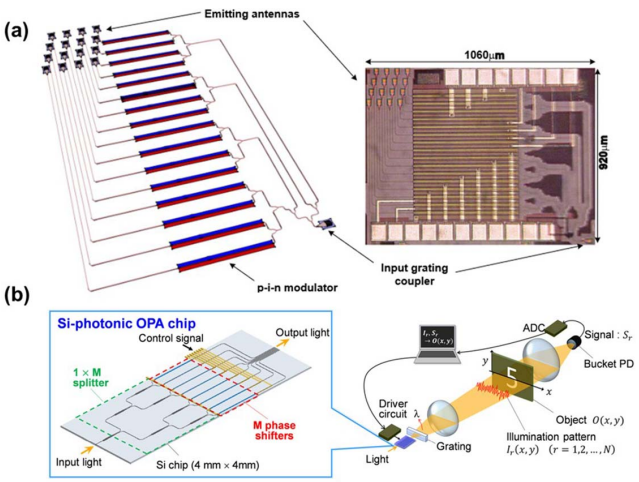

Fig. 21. (a) Nanophotonic projection system[47]. (b) Schematic of GI system using an integrated OPA chip[48].

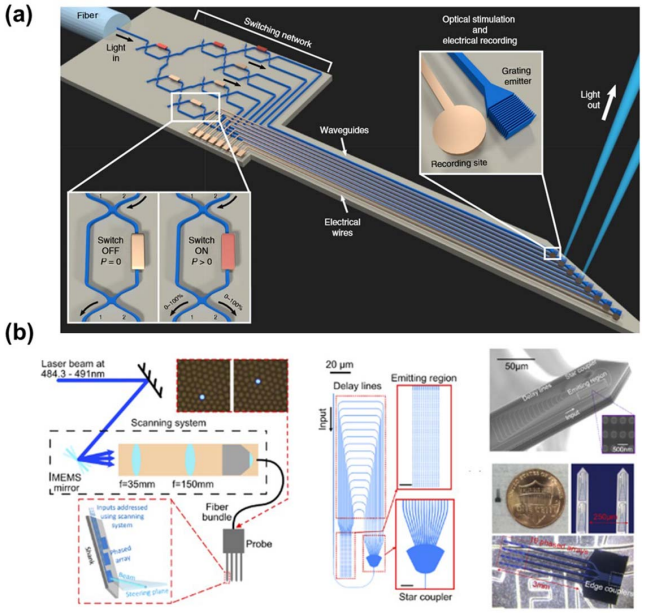

Fig. 22. (a) Schematic of an implantable probe based on reconfigurable nanophotonics[50]. (b) Schematic of the OPA neural probe connected to the scanning system[51].

neural stimulation and recording, can be employed for biosensing applications.

Mohanty *et al.* have demonstrated a design and fabrication of implantable silicon-based probes composed of SiN array waveguides[50], as shown in Fig. 22(a). These probes enable rapid reconfiguration and routing of multiple beams through electrical tuning. In mice experiments, these probes have shown the capability of stimulating small groups of individual neurons with sub-millisecond precision, generating multi-neuronal spike patterns. Subsequently, Sacher *et al.* extended the use of SiN OPAs as optical emitters[51], as shown in Fig. 22(b), controlling emitted beams through wavelength tuning. These probes were validated in mice brain slices, proving to have sufficient power for optogenetic stimulation and functional imaging while allowing control of the spatial distribution of beams at the neuronal scale.

These studies indicate that reconfigurable silicon-based optical probes based on OPAs can be used for structured illumination, focusing, and steering in deep brain regions. This opens up new possibilities for achieving high-resolution functional imaging in neuroscience research.

5.5. Specialized beam generation

Specialized beams have unique advantages in areas such as communication, imaging, sensing, and optical tweezers. Large-scale OPA technology, owing to its capacity for flexible optical field control, particularly excels in generating specialized beams.

Du *et al.* introduced a straightforward and compact on-chip optical vortex lattice emitter employing a tilt grating array[52], as illustrated in Fig. 23(a). Their work enabled the on-chip versatile

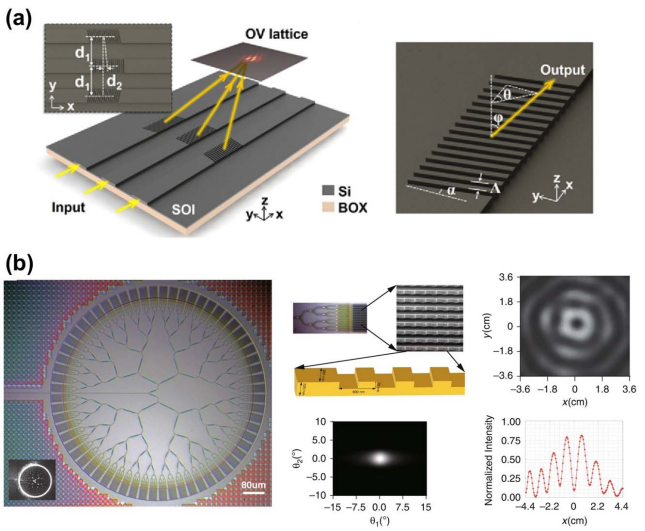

Fig. 23. (a) On-chip optical vortex lattice emitter[52]. (b) On-chip Bessel–Gaussian beam generator[53].

emission of optical vortices, leveraging the principle of three-plane-wave interference. This development opens up opportunities for creating, controlling, and detecting optical vortex lattices through photonic integrated circuits. In order to achieve larger-scale specialized beam generation, Zhi *et al.* proposed a photonic integrated chip, incorporating concentrically arranged grating arrays for on-chip generation of Bessel beams[53], as shown in Fig. 23(b). They measured light spots with Bessel function curves at a distance of 10.24 m. Leveraging the rotational Doppler effect, they successfully measured the rotation speed of a rotating object experimentally, with a maximum error of only 0.05%.

These studies underscore the promising future of large-scale OPA technology in specialized beam generation, offering crucial support for innovation and practical applications that leverage unique optical properties.

6. Conclusion and Outlook

In this paper, we summarized the development of OPAs and photonic integrated LiDAR. Thanks to the mature CMOS fabrication technology, large-scale integrated OPAs made on a silicon photonic platform would be commercialized in the future for solid-state LiDAR devices. Current OPAs could achieve a sharp IFoV and a wide FoV, but the relatively high on-chip loss and nonlinear absorption still limit the radiated power and detection range. 3D integration provides a way to define different functional layers and to form a large coherent aperture. At the same time, further improvement of the fabrication process will promote the performance of the active OPAs, making it more suitable for complex environments and applications. With hybrid integration of an on-chip light source and amplifier, it is more advantageous to push the OPAs from laboratory demo to commercial applications, including vehicle LiDAR, imaging, sensing, and FSO.

Acknowledgements

This work was supported by the Key Research and Development Program of Hubei Province (No. 2021BAA004), the Innovation Project of Optics Valley Laboratory (Nos. OVL2021BG004 and OVL2023ZD004), the National Natural Science Foundation of China (NSFC) (Nos. 62125503, 62261160388, and 62105115), and the Natural Science Foundation of Hubei Province of China (No. 2023AFA028).

References

1. L. Wu, X. Wang, X. He, *et al.*, "Arbitrary multiple beam forming by two cascaded liquid crystal optical phased arrays," Opt. Express **26**, 17066 (2018).
2. X. He, X. Wang, L. Wu, *et al.*, "Aperture scalable liquid crystal optically duplicated array of phased array," Opt. Commun. **451**, 174 (2019).
3. M. R. Kossey, C. Rizk, and A. C. Foster, "End-fire silicon optical phased array with half-wavelength spacing," APL Photonics **3**, 011301 (2017).
4. M. Chul Shin, A. Mohanty, K. Watson, *et al.*, "Chip-scale blue light phased array," Opt. Lett. **45**, 1934 (2020).
5. K. Van Acoleyen, W. Bogaerts, J. Jágerská, *et al.*, "Off-chip beam steering with a one-dimensional optical phased array on silicon-on-insulator," Opt. Lett. **34**, 1477 (2009).
6. J. C. Hulme, J. K. Doylend, M. J. R. Heck, *et al.*, "Fully integrated hybrid silicon two dimensional beam scanner," Opt. Express **23**, 5861 (2015).
7. C. V. Poulton, A. Yaacobi, D. B. Cole, *et al.*, "Coherent solid-state LIDAR with silicon photonic optical phased arrays," Opt. Lett. **42**, 4091 (2017).
8. C. V. Poulton, M. J. Byrd, P. Russo, *et al.*, "Coherent LiDAR with an 8,192-element optical phased array and driving laser," IEEE J. Sel. Top. Quantum Electron. **28**, 6100508 (2022).
9. X. Yan, J. Chen, D. Dai, *et al.*, "Polarization multiplexing silicon-photonic optical phased array for 2D wide-angle optical beam steering," IEEE Photonics J. **13**, 6600506 (2021).
10. N. A. Tyler, D. Fowler, S. Malhouitre, *et al.*, "SiN integrated optical phased arrays for two-dimensional beam steering at a single near-infrared wavelength," Opt. Express **27**, 5851 (2019).
11. S. Zhao, J. Chen, and Y. Shi, "Dual polarization and bi-directional silicon-photonic optical phased array with large scanning range," IEEE Photonics J. **14**, 6620905 (2022).
12. Y. Zhang, Y.-C. Ling, K. Zhang, *et al.*, "Sub-wavelength-pitch silicon-photonic optical phased array for large field-of-regard coherent optical beam steering," Opt. Express **27**, 1929 (2019).
13. P. Wang, G. Luo, Y. Xu, *et al.*, "Design and fabrication of a SiN-Si dual-layer optical phased array chip," Photonics Res. **8**, 912 (2020).
14. Y. Li, B. Chen, Q. Na, *et al.*, "Wide-steering-angle high-resolution optical phased array," Photonics Res. **9**, 2511 (2021).
15. G. Yue and Y. Li, "Integrated lithium niobate optical phased array for two-dimensional beam steering," Opt. Lett. **48**, 3633 (2023).
16. Z. Wang, W. Song, Y. Chen, *et al.*, "Metasurface empowered lithium niobate optical phased array with an enlarged field of view," Photonics Res. **10**, B23 (2022).
17. J. Sun, E. Timurdogan, A. Yaacobi, *et al.*, "Large-scale nanophotonic phased array," Nature **493**, 195 (2013).
18. F. Ashtiani and F. Aflatouni, "*N*×*N* optical phased array with 2*N* phase shifters," Opt. Express **27**, 27183 (2019).
19. C. Rogers, A. Y. Piggott, D. J. Thomson, *et al.*, "A universal 3D imaging sensor on a silicon photonics platform," Nature **590**, 256 (2021).
20. X. Zhang, K. Kwon, J. Henriksson, *et al.*, "A large-scale microelectromechanical-systems-based silicon photonics LiDAR," Nature **603**, 253 (2022).
21. K. Van Acoleyen, K. Komorowska, W. Bogaerts, *et al.*, "One-dimensional off-chip beam steering and shaping using optical phased arrays on silicon-on-insulator," J. Lightwave Technol. **29**, 3500 (2011).
22. C. V. Poulton, M. J. Byrd, P. Russo, *et al.*, "Long-range LiDAR and free-space data communication with high-performance optical phased arrays," IEEE J. Sel. Top. Quantum Electron. **25**, 7700108 (2019).
23. S. A. Miller, Y.-C. Chang, C. T. Phare, *et al.*, "Large-scale optical phased array using a low-power multi-pass silicon photonic platform," Optica **7**, 3 (2020).

24. K. Van Acoleyen, H. Rogier, and R. Baets, "Two-dimensional optical phased array antenna on silicon-on-insulator," Opt. Express **18**, 13655 (2010).
25. H. Abediasl and H. Hashemi, "Monolithic optical phased-array transceiver in a standard SOI CMOS process," Opt. Express **23**, 6509 (2015).
26. G. Kang, C.-H. Youn, K. Yu, *et al.*, "Silicon-based optical phased array using electro-optic p-i-n phase shifters," IEEE Photon. Technol. Lett. **31**, 1685 (2019).
27. W. Xie, T. Komljenovic, J. Huang, *et al.*, "Heterogeneous silicon photonics sensing for autonomous cars [Invited]," Opt. Express **27**, 3642 (2019).
28. T. Hiraki, T. Aihara, K. Hasebe, *et al.*, "Heterogeneously integrated III–V/Si MOS capacitor Mach–Zehnder modulator," Nat. Photonics **11**, 482 (2017).
29. K. Shang, C. Qin, Y. Zhang, *et al.*, "Uniform emission, constant wavevector silicon grating surface emitter for beam steering with ultra-sharp instantaneous field-of-view," Opt. Express **25**, 19655 (2017).
30. L. Yu, P. Ma, G. Luo, *et al.*, "Adoption of large aperture chirped grating antennas in optical phase array for long distance ranging," Opt. Express **30**, 28112 (2022).
31. M. Raval, C. V. Poulton, and M. R. Watts, "Unidirectional waveguide grating antennas with uniform emission for optical phased arrays," Opt. Lett. **42**, 2563 (2017).
32. S. Suyama and T. Baba, "High-efficiency upward radiation in a slow-light grating beam scanner," Opt. Express **31**, 22170 (2023).
33. H. Park, Y.-H. Kuo, A. W. Fang, *et al.*, "A hybrid AlGaInAs-silicon evanescent preamplifier and photodetector," Opt. Express **15**, 13539 (2007).
34. I. Kim, R. J. Martins, J. Jang, *et al.*, "Nanophotonics for light detection and ranging technology," Nat. Nanotechnol. **16**, 508 (2021).
35. W. Song, R. Gatdula, S. Abbaslou, *et al.*, "High-density waveguide superlattices with low crosstalk," Nat. Commun. **6**, 7027 (2015).
36. Y. Liu and H. Hu, "Silicon optical phased array with a 180-degree field of view for 2D optical beam steering," Optica **9**, 903 (2022).
37. J. He, T. Dong, and Y. Xu, "Review of photonic integrated optical phased arrays for space optical communication," IEEE Access **8**, 188284 (2020).
38. S. Chung, H. Abediasl, and H. Hashemi, "A monolithically integrated large-scale optical phased array in silicon-on-insulator CMOS," IEEE J. Solid-State Circuit **53**, 275 (2018).
39. H. Qiu, Y. Liu, X. Meng, *et al.*, "Bidirectional high sidelobe suppression silicon optical phased array," Photonics Res. **11**, 659 (2023).
40. Y. Kim, H. Yoon, J.-B. You, *et al.*, "Wide-angle beam-steering using an optical phased array with non-uniform-width waveguide radiators," Photonics **7**, 56 (2020).
41. D. Kwong, A. Hosseini, Y. Zhang, *et al.*, "1 × 12 Unequally spaced waveguide array for actively tuned optical phased array on a silicon nanomembrane," Appl. Phys. Lett. **99**, 051104 (2011).
42. D. N. Hutchison, J. Sun, J. K. Doylend, *et al.*, "High-resolution aliasing-free optical beam steering," Optica **3**, 887 (2016).
43. Y. Jin, J. Wu, A. Yan, *et al.*, "Optimum beam steering of optical phased arrays using mixed weighting technique," Optik **125**, 4568 (2014).
44. W. Xu, Y. Guo, X. Li, *et al.*, "Fully integrated solid-state LiDAR transmitter on a multi-layer silicon-nitride-on-silicon photonic platform," J. Light. Technol. **41**, 832 (2023).
45. C.-W. Chow, Y.-C. Chang, S.-I. Kuo, *et al.*, "Actively controllable beam steering optical wireless communication (OWC) using integrated optical phased array (OPA)," J. Light. Technol. **41**, 1122 (2023).
46. Y. Li, B. Chen, Q. Na, *et al.*, "High-data-rate and wide-steering-range optical wireless communication via nonuniform-space optical phased array," J. Light. Technol. **41**, 4933 (2023).
47. F. Aflatouni, B. Abiri, A. Rekhi, *et al.*, "Nanophotonic projection system," Opt. Express **23**, 21012 (2015).
48. Y. Kohno, K. Komatsu, R. Tang, *et al.*, "Ghost imaging using a large-scale silicon photonic phased array chip," Opt. Express **27**, 3817 (2019).
49. J. Yoon, H. Yoon, J.-Y. Kim, *et al.*, "Demonstration of high-accuracy 3D imaging using a Si optical phased array with a tunable radiator," Opt. Express **31**, 9935 (2023).
50. A. Mohanty, Q. Li, M. A. Tadayon, *et al.*, "Reconfigurable nanophotonic silicon probes for sub-millisecond deep-brain optical stimulation," Nat. Biomed. Eng. **4**, 223 (2020).
51. W. D. Sacher, F.-D. Chen, H. Moradi-Chameh, *et al.*, "Optical phased array neural probes for beam-steering in brain tissue," Opt. Lett. **47**, 1073 (2022).
52. J. Du and J. Wang, "Chip-scale optical vortex lattice generator on a silicon platform," Opt. Lett. **42**, 5054 (2017).
53. Z. Zhi, Q. Na, Q. Xie, *et al.*, "On-chip generation of Bessel–Gaussian beam via concentrically distributed grating arrays for long-range sensing," Light Sci. Appl. **12**, 92 (2023).